Heliyon 9 (2023) e18219

Contents lists available at ScienceDirect

Heliyon

journal homepage: www.cell.com/heliyon

# Influence of base material particle features on petrophysical properties of synthetic carbonate plugs

Jhonatan Jair Arismendi Florez [a,*], Mateus Michelon [b], Carina Ulsen [a], Jean Vicente Ferrari [a]

[a] Escola Politécnica da Universidade de São Paulo – Departamento de Engenharia de Minas e Petróleo, Av. Professor Mello Moraes, 2603, 05508-030, São Paulo, Brazil
[b] Petrobras S.A, Gerencia Geral de Exploração, Av. Henrique Valadares, 28, 20231-030, Rio de Janeiro, Brazil

ARTICLE INFO

*Keywords:*
Petrophysical properties
Synthetic carbonate plugs
Controlled pore network

ABSTRACT

Rocks with representative physical and chemical properties are essential to understanding fluid-solid flow behaviors at the pore scale. In this way, studying the pore space characteristics is a key point for evaluating and providing petrophysical properties for distinct rock types, such as synthetic rocks, with controlled and representative properties like natural ones. This work studies the petrophysical properties of synthetic carbonate plugs with a novel approach by correlating particle size, particle size fraction, and the morphology of particles with porosity and permeability, which could guide the scientific community to further forming of carbonate rocks with a controlled pore network. Results indicated that particle shape influenced the accommodation of particles in the porous space and, therefore, in the petrophysical properties, where an increase in particle size decreases porosity and increases permeability. Also, the obtained plugs showed the following petrophysical features: gas porosity from 10% to 17%, mercury porosity from 11% to 19%, gas permeability from 0.07 mD to 0.70 mD, and mercury permeability from 0.02 mD to 0.35 mD, providing important insight on controlling pore space in synthetic carbonate rocks.

## 1. Introduction

The pore structure of carbonate rocks can be modified by post-depositional dissolution, recrystallization, cementation, dolomitization, and substitution by other minerals [1] apud [2]. Chemical processes alter primary interparticle pores during the early diagenetic stage, forming larger secondary pores such as vugs randomly distributed with different scales/densities per unit area [3]. Combined with complex porosity, these attributes result in heterogeneous reservoirs, hence giving rise to significant challenges to data acquisition, petrophysical evaluation, and reservoir description [4,5]. These reservoir property evaluations are one of the major concerns for hydrocarbon exploration and production [6,7].

Bust [8] recommend considering the following key parameters to understand the pore geometry of carbonates: the pore size and the pore-coordination number. Sing [9] apud Lowell [10] described a pore size classification proposed by The International Union of Pure and Applied Chemistry based on the internal pore width: pores with an internal width less than 0.002 μm are micropores; pores with an internal width between 0.002 and 0.05 μm are mesopores, and pores with an internal width greater than 0.05 μm are macropores. However, Schlumberger [11] proposes a pore size classification for carbonate rocks from oil fields: pores with an internal width less

* Corresponding author.
*E-mail address:* jhonatanarismendi@usp.br (J.J. Arismendi Florez).

https://doi.org/10.1016/j.heliyon.2023.e18219
Received 4 May 2023; Received in revised form 11 July 2023; Accepted 12 July 2023
Available online 15 July 2023

than 0.5 μm are micropores; pores with an internal width between 0.5 and 5 μm are mesopores, and pores with an internal width greater than 5 μm are macropores.

Porosity may be described as the ratio of the void volume (pores) to the total volume of the rock. Depending on the interconnectivity of these void volumes, porosity can be expressed as effective (volume of interconnected voids/pores) or total (volume of all the voids/pores, regardless of their interconnection) [12]. In addition, based on the interconnection of pores, liquids or gases can easily pass through a material. The measure of this passage is called permeability [13]. In Brazil, The National Agency of Petroleum, Natural Gas and Biofuels (ANP), reported that some of the Brazilian pre-salt oil fields have between 6 and 28% of effective porosities and 0.1 to 10,000 mD permeabilities [14–22]. This high variability is consistent with the well-known complex pore system of natural carbonate rocks [23,24] that can pose a challenge to be controlled in synthetic rocks.

Hook [25] mentioned some factors which control porosity: particle size distribution, the morphology of particles, compaction, and cementation. In this work, such factors are approached.

According to Church [26], particle size determines the absolute magnitude of a particle derived from reference to an external metric. The diameter can describe the size of spherical particles because of its identical dimension. However, rocks are formed by non-spherical particles (particles with multiple lengths and widths). A lot of particle size techniques assume that every particle is a sphere. In this sense, physical measurements determine the sphere's size to produce the data [27]. Particles are commonly classified by their diameters: gravel from 60 mm to 2 mm, sand from 2 mm to 0.06 mm, silt from 0.06 mm to 0.002 mm, and clay $<$0.002 mm [28,29].

The morphology of particles may vary systematically with particle size [30]. It is known that in an ideal case of a rock with a known bulk volume conformed by ideal uniform homogeneous spherical particles, the porosity is independent of the size of the particle, and its value is the highest possible to obtain. However, natural rocks are formed by heterogeneous particles with different sizes and morphology. These properties affect the packing of the particles in the bulk volume and therefore change the porosity and permeability of the rock. The larger the particle's sphericity, the greater the porosity of the solid [25,31].

Massad [28] defines compaction as the reduction of voids between particles due to mechanical and chemical processes, causing compression or pore air expulsion and, therefore, an increase in the density of the sample. The mechanical processes are controlled by effective stress and the chemical compaction by dissolution and precipitation of solids (a function of thermodynamics and kinetics; therefore, this process is very slow and sensitive to temperature) [32]. Small liquid flow channels and low flow rates are characteristic of compact rock due to the dense structure and small pore-throat radius [33]. Rock compaction can be influenced by mineral composition, rock texture and structure, rock density, weathering degree, and water conditions [34]. In carbonates, mechanical compaction can be reduced by cement or bonding materials [35]. On carbonates, the precipitation of minerals acts as a bonding material, which can be located around particles filling the pores with sediment, causing cementation and reductions in porosity and permeability [36].

In cases where reservoir samples cannot be obtained, synthetic rocks offer a closer approximation due to their controllable chemical and physical characteristics [31,37–39].

Arismendi [31] reviewed 81 scientific studies published between 1962 and 2016. The review provides an extensive overview of the construction methods and recent advancements in producing synthetic carbonate plugs. The authors discuss the significance of synthetic plugs in studying reservoir properties and the challenges associated with obtaining natural rock samples. The authors also discuss the importance of accurately replicating natural carbonate rocks' physical and chemical properties in synthetic plugs and the lack of work concerning methodologies to construct these samples.

From 2016 until now, some developments have been published to contribute to this area. For example, Morais [38] comprehensively analyzes the sintering and carbonation processes for obtaining bulk calcium carbonate samples. The research explores successful and failed attempts in fabricating calcium carbonate samples using these methods. It presents the results of successful attempts, where bulk calcium carbonate samples with desired properties were successfully obtained from controlled sintering and carbonation. These successful cases demonstrate the potential of these methods for producing high-quality calcium carbonate structures. Additionally, this work discusses the reasons behind failed attempts, highlighting the factors that hinder the successful fabrication of bulk calcium carbonate samples. These factors include inadequate sintering conditions, poor material preparation, and variations in process parameters.

Then, based on its successful attempts, Morais [39] presents a detailed study on the fabrication and petrophysical characterization of artificial carbonate rocks with multiscale porosity using a sintering process conducted in a $CO_2$ atmosphere. The authors reported that obtained samples presented high mechanical resistance (40–126 MPa), therefore, a good consolidation and resistance to water immersion, in addition to controlled porosity and pore size distribution. The petrophysical characterization included measurements of porosity at different scales, including macro-, meso-, and micro-porosity, using advanced imaging techniques such as X-ray micro-computed tomography and nuclear magnetic resonance. The obtained samples had some limitations regarding petrophysics features related to low permeabilities and a poorly connected porous network, with closed inter and intra-granular pores that were not connected to the exterior of the sample, likely resulting from the employed sintering consolidation method. Besides, as in the case of this present work, the mineral sample composition of Morais [39] was based on calcium carbonate. However, carbonate reservoir rock is additionally composed of quartz and dolomite.

Arismendi [37] published a promising methodology to construct synthetic carbonate plugs and an in-depth examination by evaluating consolidation, basic petrophysical, and wettability properties comparable to those found in natural rocks from carbonate reservoirs. The work suggested a modified approach to existing methodologies, which involves subjecting pulverized carbonate rocks with varying particle sizes to uniaxial compaction while manipulating temperature and pH levels.

The constructed samples exhibited favorable consolidations and desirable porosity, permeability, and surface wettability

characteristics. The contact angle measurements indicated intermediate wettability, with angles obtained with water drop ranging from 50 to 80° (intermediate-wet) and greater than 80° for oil-wet conditions. These results align with the characteristics observed in certain Brazilian pre-salt oilfields. Based on the results of this work, the authors highlighted the need for two dedicated follow-up studies. The first study would investigate the wettability properties in more detail, while the second study would explore the petrophysical properties of the constructed samples.

Regarding wettability, the initial basic wettability tests conducted provided a preliminary understanding of the surface behavior of the constructed synthetic rocks. However, more complete wettability tests, such as the Amott-Harvey method, are required for a more comprehensive analysis. These tests will allow a deeper investigation into the influence of various sample properties affecting wettability alteration, including pore roughness, sample mineralogy, and other relevant factors, on the wettability characteristics of the synthetic rocks.

From a basic petrophysical perspective, the initial assessment of porosity and permeability provided an understanding of the pore characteristics in the constructed synthetic rocks. However, a comprehensive understanding of the relationship between the properties of the base materials used in the rock formation and the control of the resulting rock's pore network has not been established. Therefore, it is crucial to investigate further and comprehend these relationships to understand how the properties of the starting (base) materials influence the pore network of synthetic rocks.

In light of the mentioned research gap, the present study addressed only the petrophysical aspect, and no analysis was developed regarding the wettability issue. Based on the suggested plug composition and methodology proposed by Arismendi [37], synthetic plugs were fabricated to establish a correlation between the plugs' pore network and the base material's particle characteristics. The primary focus of this work was to investigate how the particle features of the base material influence the petrophysical properties of synthetic carbonate plugs. The present work and the previously published findings on consolidation and wettability [37] contribute to a deeper understanding of synthetic carbonate plugs. The insights gained from this study may aid future research endeavors to replicate rocks resembling natural carbonate rocks found in reservoirs.

To obtain an understanding of the geophysical parameters, covering a wide range of material, and pore characterization, in this work, samples were analyzed experimentally by destructive and non-destructive methodologies, as follows: gas expansion porosimetry, mercury intrusion porosimetry, scanning electron microscopy, and X-ray micro-computed tomography. Herein, some of the well-known limitations of the adopted methodology for determining geophysical parameters and how they were addressed in this work are presented. Additionally, each of these methodologies are fully explained in the methodology section.

1. Gas expansion porosimetry involves measuring the pore volume by allowing the gas within the pores to expand into a known volume while monitoring the associated pressure changes. This technique provides an absolute measure of connected porosity and permeability but does not provide detailed information about the pore size distribution. Thus, to better understand the pore network, it is important to use complementary techniques, such as mercury porosimetry, allowing a more detailed analysis of the sample's pore size distribution range.
2. Mercury porosimetry is a destructive analysis due to the mercury intrusion in the sample, in which the sample dimension is limited by the size of the sample holder (penetrometer). If the samples to be analyzed contain a controlled base material homogeneously distributed, smaller subsamples can be obtained, representing the larger ones to meet the sample size limitation of this technique, which was the approach adopted in this work, as will be explained in the methodology section.
3. The connection between the length-scale and image resolution determines the constraint of microtomography. When aiming for higher resolution, it is common to scan a smaller length-scale. Therefore, this study employed two resolutions to examine samples from both macro- and micro-scale perspectives in a tentative to address the image resolution limitations.
4. The total porosity of rock samples comprises connected and unconnected porosity. This work demonstrates a strong correlation between destructive and non-destructive methodologies, enabling the investigation of the pore network. Nevertheless, additional techniques, such as nuclear magnetic resonance (NMR), are available to enhance the understanding of the pore network, but this technique was not applied to this work.

## 2. Methodology

This work utilized the guidelines proposed and recommended compositions to construct synthetic plugs published by Arismendi [37]. It includes the compaction by uniaxial compression of pulverized carbonate rock with controlled particle sizes and mass composition ratios 50%w/w:50%w/w (<0.02 mm:0.02–0.074 mm and 0.15mm–0.3 mm:0.3–0.6 mm) and amide wax under varying temperature and pH conditions.

To establish a correlation between the plug's pore network and its base material, a wider range of particle sizes was used in addition to those suggested by Arismendi [37]. In this way, the following particle sizes and mass composition ratios were also used 50% w/w:50%w/w (0.02–0.074 mm:0.074–0.15 mm; 0.074–0.15 mm:0.15–0.3 mm) and 25%w/w:75%w/w (<0.02 mm:0.02–0.074 mm; 0.02–0.074 mm:0.074–0.15 mm; 0.074–0.15 mm:0.15–0.3 mm; 0.15mm–0.3 mm:0.3–0.6 mm).

The samples were formed using a dolomite rock with a controlled particle size as the base material, mimicking a natural matrix rock. The consolidation was improved by adding an amide wax powder of type $C_{38}H_{76}N_2O_2$ as a bonding material (5%w/w relative to the base material). Additionally, a hydrogen chloride solution with pH 3 (6%w/w relative to the base material) was utilized because of its acidic nature, increasing calcium carbonate's solubility. As a result, the base material dissolves, followed by precipitation upon heating to a temperature of 100 °C. Table 1 describes the synthetic plug materials and their content.

**Table 1**
Description of the synthetic plug materials and their content.

| Material/ procedure | Function | Description | Content |
|---|---|---|---|
| Dolomite | Base material | Dolomite with a grain density of 2.87 g/ cm3 | 100 g (34.8 $cm^3$) |
| Bonding material | Enhance consolidation of the samples | Amide wax of type $C_{38}H_{76}N_2O_2$ with a specific gravity of 1.0 | 5% w/w (14.4% v/v) corresponding to the base material |
| Acid solution | Increase calcium carbonate solubility, causing a dissolution of base material | hydrogen chloride solution of pH 3 | 6% w/w (17.22% v/v) corresponding to the base material |
| Temperature | Cause precipitation of the previously acid-dissolved base material | Oven with air circulation | One at 100 °C |

**Table 2**
Composition of each constructed sample.

| Sample | Base material | | | | | | Bonding material (% w/w relative to 100 g of base material) | hydrogen chloride solution of pH 3 (% w/w relative to 100 g of base material) |
|---|---|---|---|---|---|---|---|---|
| | Total quantity of base material (g) | 100 g of base material composed in Weight fraction by (%) | | | | | | |
| | | 0.3–0.6 mm | 0.15–0.3 mm | 0.074–0.15 mm | 0.02–0.074 mm | <0.02 mm | | |
| 1 | 100 | | | | 50 | 50 | 5 | 6 |
| 2 | 100 | | | | 50 | 50 | 5 | 6 |
| 3 | 100 | | | 50 | 50 | | 5 | 6 |
| 4 | 100 | | | 50 | 50 | | 5 | 6 |
| 5 | 100 | | 50 | 50 | | | 5 | 6 |
| 6 | 100 | | 50 | 50 | | | 5 | 6 |
| 7 | 100 | 50 | 50 | | | | 5 | 6 |
| 8 | 100 | 50 | 50 | | | | 5 | 6 |
| 9 | 100 | | | | 75 | 25 | 5 | 6 |
| 10 | 100 | | | | 75 | 25 | 5 | 6 |
| 11 | 100 | | | 75 | 25 | | 5 | 6 |
| 12 | 100 | | | 75 | 25 | | 5 | 6 |
| 13 | 100 | | 75 | 25 | | | 5 | 6 |
| 14 | 100 | | 75 | 25 | | | 5 | 6 |
| 15 | 100 | 75 | 25 | | | | 5 | 6 |
| 16 | 100 | 75 | 25 | | | | 5 | 6 |

### 2.1. Base material preparation and characterization

The dolomite outcrop utilized as a base material underwent X-ray diffraction analysis, revealing its mineralogical composition as dolomite, calcite, tremolite, and quartz. Moreover, the primary chemical composition, as determined by standardless X-ray fluorescence, and involving the elemental analysis between fluorine and uranium, showed a composition of 36.4% CaO, 15.5% MgO, 4.51% SiO2, and 41.9% LOI (loss on ignition at 1020 °C).

The dolomite outcrops were broken down into smaller particles using a jaw crusher (BM 2010) and a roller crusher (Furlan MR2515). The resulting particles were then sorted according to their size using a mechanical sieve (Haver EML digital plus sieve), with a sorting duration of 20 min, an interval of 15 s, and a wavelength of 14 Hz. Four particle size intervals were obtained, namely 0.3–0.6 mm, 0.15–0.3 mm, 0.074–0.15 mm, and 0.02–0.074 mm. A subsample of particles within the 0.02–0.074 mm range was pulverized for 2 min using a Herzog pulverizer before resorted in the same digital sieve, which yielded particles smaller than <0.02 mm.

Furthermore, the five particle size intervals were analyzed for their particle size distribution in terms of the minimum particle diameter (xc_min) and particle shape characteristics such as Feret diameter (b/l) and sphericity (SPHT) using laser light scattering in a Camsizer-XT (CAM). The b/l and SPHT values are used to determine the degree of deviation from an ideal sphere, where a value of 1 indicates a perfect sphere, while values lower than 1 indicate a deviation from a perfect sphere [40].

### 2.2. Forming synthetic carbonate plugs

The formation of samples with plug geometry involved using 100 g of the sorted base material in the weight fractions of 50% w/w:50% w/w (samples 1 to 8) or 25% w/w: 75%w/w (samples 9 to 16). Next, amide wax powder $C_{38}H_{76}N_2O_2$ (5%w/w relative to 100 g of base material) and a hydrogen chloride solution of pH 3 (6% w/w relative to 100 g of base material) were added and mixed for 1 min. The resulting blend was then compressed uniaxially with a load force of 200 kN and a 25 mm/min constant velocity. After compression, the plug was dried at 100 °C and cooled to room temperature (27–30 °C). Table 2 displays the composition of each sample constructed.

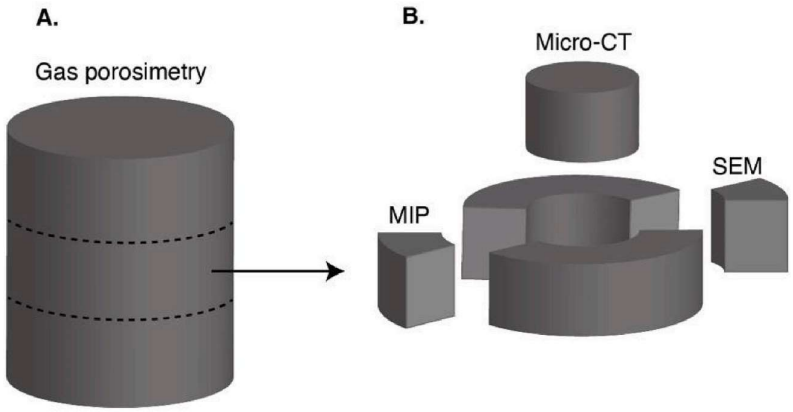


**Fig. 1.** vol and sub-volumes from synthetic plugs analyzed by experimental tests such as gas porosimetry (part A), micro-CT, MIP, and SEM (part B).

### *2.3. Characterization of the synthetic carbonate plugs*

#### *2.3.1. Calculated porosity*

The synthetic carbonate plugs were subjected to measurements of their diameter (in cm), height (in cm), and mass (in g) by taking three readings and reporting the average. A caliper with a precision of 0.01 cm and an analytical balance with an accuracy of 0.0001 g were utilized for the measurements. To determine the porosity of the plugs, Equation 1 was applied, which involves calculating the plug's volume $v$ (in $cm^3$) using the measured diameter and height, obtaining the grain density $\rho$ (in $g/cm^3$) by gas or mercury porosimetry analysis, and utilizing the plug's mass $m$. The computed porosity $\varnothing$ values were then used to compare and gain a better understanding of the experimental porosity results obtained from gas and mercury analysis.

$$\varnothing(\%) = \frac{v.\rho - m}{v.\rho} \times 100$$

#### *2.3.2. Gas expansion porosimetry measurements*

It was used in an Ultrapore300 porosimeter and Ultraperm500 permeameter at a confinement pressure of 2400 psi. The plugs' porosity, absolute permeability, and grain density were determined by the injection of nitrogen into the entire volume of the synthetic plugs (see Fig. 1A). Before the test, the synthetic plugs were dried at 60 °C and 45% humidity for 24 h. The reported permeability was absolute, corrected from the Klinkerberg effect. The slippage factor used was from Jones [41]. These measurements provided valuable insights into the porosity and permeability properties of the synthetic plugs.

#### *2.3.3. Mercury intrusion porosimetry (MIP)*

The pore characteristics of the plugs were analyzed using a Micromeritics AutoPore IV mercury porosimeter, which measured the pore size distribution, porosity, permeability, and grain density. The analysis was carried out on small subvolumes of the plug measuring 0.5 cm × 0.5 cm x 0.3 cm (see Fig. 1B), and pore pressure ranges from 0.5 to 40,000 psi were used. The Washburn equation was employed to calculate the pore size distribution, assuming cylindrical pores. The equation converted the imposed pressure $p$ into the corresponding pore radius $r$, using parameters such as the mercury contact angle $\theta$ (130°) and surface tension $\gamma$ (485 mNm-1) (Equation 2) [42].

$$p = \frac{2\gamma \cos \cos \theta}{r}$$

#### *2.3.4. Scanning eléctron microscopy (SEM) and energy dispersive spectroscopy (EDS)*

The surface of a plug fragment measuring 0.5 cm × 0.5 cm x 0.3 cm (as shown in Fig. 1B) was imaged using a Stereoscan 440 scanning electron microscope at a 1000× magnification after it was cold-mounted (embedded) in epoxy resin. Backscattered and secondary electron images were obtained to determine microstructures and identify microelements present on the surface of the plug fragments, ranging from Berllium to Americium.

#### *2.3.5. X-ray micro-computed tomography (micro-CT)*

The X-ray micro-computed tomography (micro-CT) Xradia Versa xrm 510 was employed to visualize the internal structure of the synthetic plugs, as a non-destructive method, based on variations in density and atomic composition of elements. A cylindrical sub-sample of 1 cm diameter and 1 cm height extracted from the synthetic plug was analyzed (Fig. 1B). Two microtomography analyses were employed in this work: a macro analysis to study the internal distribution of the bonding material and a micro analysis to study the pore distribution. Table 3 presents the acquisition conditions for both studies.

**Table 3**
X-ray micro-computed tomography acquisition conditions.

| Parameters | Macro condition analysis | Micro condition analysis |
|---|---|---|
| Objective | 0.39× | 4× |
| Source settings | 80 kV-7W | 80 kV-7W |
| Pixel size (μm) | 20.5 | 2.0 |
| Number of projections | 1000 | 1000 |
| Time per projection (s) | 2 | 5 |
| Resolution detector | 1024 × 1024 | 1024 × 1024 |
| FOV (μm) | 21,020 | 2051 |
| Transmission (%) | 27 | 15 |
| Source position (mm) | 38 | 18 |
| Detector position (mm) | 87 | 42 |

**Table 4**
Particle size and morphology of the obtained disintegrated dolomite rock outcrops by CAM technique.

| Particle size range from mechanical sieve (mm) | Particle size and morphology from light scattering measurement (CAM) | | | | | |
|---|---|---|---|---|---|---|
| | D [10] (mm) | D [50] (mm) | D [90] (mm) | D average (mm) | SPHT average | b/l average |
| 0.3–0.6 | 0.3129 | 0.4486 | 0.6094 | 0.4526 | 0.777 | 0.651 |
| 0.15–0.3 | 0.1302 | 0.2156 | 0.3179 | 0.2198 | 0.790 | 0.649 |
| 0.074–0.15 | 0.0419 | 0.0970 | 0.1493 | 0.0967 | 0.835 | 0.690 |
| 0.02–0.074 | 0.0112 | 0.0346 | 0.0732 | 0.0343 | 0.846 | 0.721 |
| <0.02 | 0.0006 | 0.0029 | 0.0178 | 0.0032 | 0.869 | 0.726 |

Acquired images were processed using the software Avizo 9, where it was applied a non-local mean filter and then the porous network was segmented using an interactive threshold algorithm.

## 3. Results and discussion

### 3.1. Forming synthetic carbonate plugs

The particle size distribution and morphology of the disintegrated dolomite rock obtained from outcrops by the Camsizer-XT (CAM) technique are presented in Table 4.

The study found that the particle size of dolomite rock was consistent across two measurement methods - mechanical sieving and light scattering D [90] and D [10]. Additionally, the results indicated that smaller particle sizes obtained from mechanical crushing using a jaw and roller crusher exhibited higher values of SPHT and b/l. The increase in these values is likely due to the crushing process, which led to a more spherical particle shape and reduced surface irregularities in smaller particles. Therefore, mechanical crushing may be helpful to achieve a more uniform particle shape and size distribution in the base material.

After analyzing the particulate material, the synthetic rocks were formed using the methodology previously described and the composition shown in Table 2. Fig. 2 presents the photographic register of the sixteen resultant constructed cylindrical synthetic carbonate plugs.

### 3.2. Characterization of the synthetic carbonate plugs

The dimensions (diameter and height), calculated volume, and mass of the plugs are presented in Table 5. Concerning the height, it was observed that there is a decrease with the increase in the size of the particles which form the synthetic carbonate plugs. The phenomenon is probably caused by the particles' mixture, which has a broader range of sizes from the smallest to the largest particle size combination, in addition to the increase of surface irregularities in the morphology SPHT and b/l with the increase of particle size. As a result, this allows the smaller particles to fit better by the increased particle size combination, leading to better accommodation and, thus, a decrease in the height of the resulting synthetic plug.

To determine the grain density of the synthetic plugs, gas, and mercury porosimetry techniques were used [43]. Since a low-density wax was used as the bonding material to form the plugs, it was predictable that the grain density would be lower than the reported values of 2.84–2.86 g/cm$^3$ for dolomite rocks, according to Webmineral [44]. The results of the porosimetry analyses revealed that the synthetic plugs had an average grain density of 2.64 g/cm$^3$ and 2.62 g/cm$^3$ for gas and mercury porosimetry, respectively, which agrees with the expected decrease in density due to the use of the low-density wax [45].

Both calculated and experimental porosities were analyzed, and it was observed that there was a similar trend of decreasing porosity with increasing particle size used in forming the synthetic plugs. For plugs consisting of a 50% w/w particle size weight fraction, the calculated porosities based on grain density from gas porosimetry ranged from 13.00% (thickest particle size combination) to 19.88% (finest particle size combination). The calculated porosities based on grain density from mercury porosimetry ranged from 12.77% (thickest particle size combination) to 18.37% (finest particle size combination). The experimental porosities measured

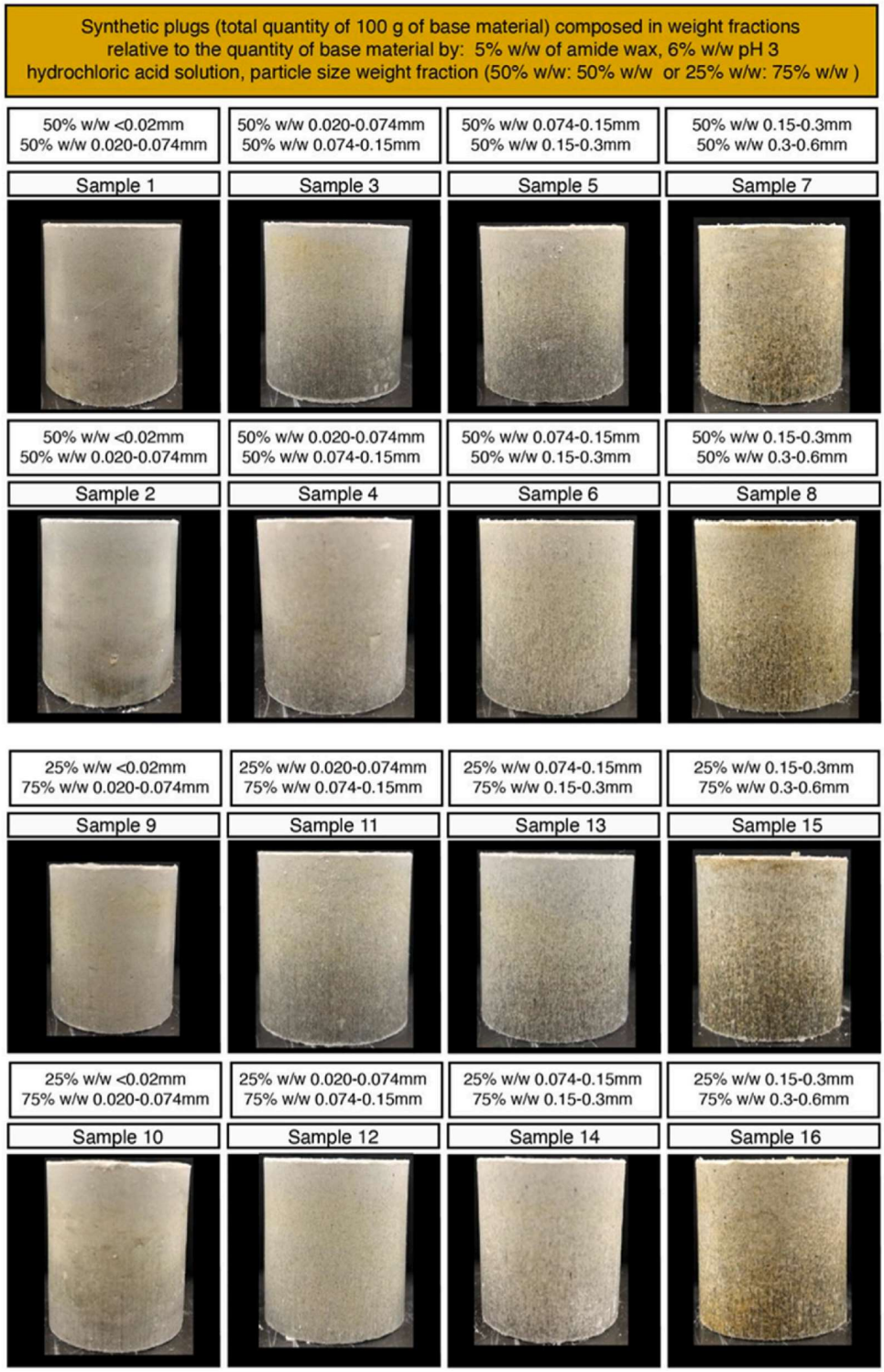


**Fig. 2.** Photographic register of the constructed sixteen cylindrical synthetic carbonate plugs.

**Table 5**
Dimensions (diameter and height), calculated volume and mass of the resultant synthetic carbonate plugs.

| | Sample | Diameter (cm) | Height (cm) | Calculated Volume ($cm^3$) | Mass (g) |
|---|---|---|---|---|---|
| | **100 g of base material mixed in weight fractions of 50% w/w: 50% w/w and 5% w/w of bonding material, 6% w/w hydrogen chloride solution of pH 3** | | | | |
| Finest particle size combination | 1 | 3.77 | 4.43 | 49.45 | 105.04 |
| | 2 | 3.77 | 4.43 | 49.45 | 104.21 |
| | 3 | 3.77 | 4.23 | 47.22 | 105.00 |
| | 4 | 3.77 | 4.22 | 47.11 | 104.17 |
| | 5 | 3.77 | 4.15 | 46.33 | 105.25 |
| | 6 | 3.77 | 4.15 | 46.33 | 104.79 |
| Thickest particle size combination | 7 | 3.77 | 4.10 | 45.77 | 104.73 |
| | 8 | 3.77 | 4.11 | 45.88 | 104.99 |
| | **100 g of base material mixed in weight fractions of 25% w/w: 75% w/w and 5% w/w of bonding material, 6% w/w hydrogen chloride solution of pH 3** | | | | |
| Finest particle size combination | 9 | 3.77 | 4.39 | 49.00 | 105.45 |
| | 10 | 3.77 | 4.40 | 49.12 | 105.52 |
| | 11 | 3.77 | 4.20 | 46.88 | 105.64 |
| | 12 | 3.77 | 4.19 | 46.77 | 104.42 |
| | 13 | 3.77 | 4.15 | 46.33 | 104.70 |
| | 14 | 3.77 | 4.15 | 46.33 | 104.39 |
| Thickest particle size combination | 15 | 3.77 | 4.06 | 45.32 | 104.41 |
| | 16 | 3.77 | 4.07 | 45.43 | 104.42 |

The synthetic plugs were subjected to petrophysical analyses to evaluate their porosity, grain density, and permeability using experimental measurements by gas and mercury porosimetry techniques. Table 6 presents these results and the calculated porosity obtained by applying Equation 1.

by gas porosimetry ranged from 10.43% (thickest particle size combination) to 17.23% (finest particle size combination). The experimental porosimetry measured by mercury porosimetry ranged from 11.27% (thickest particle size combination) to 19.96% (finest particle size combination). In all cases, the porosities tended to decrease as the particle size increased.

The calculated and experimental porosities were also analyzed for plugs with a particle size weight fraction of 25% w/w:75% w/w. The calculated porosities based on grain density from gas porosimetry ranged from 12.74% (thickest particle size combination) to 18.62% (finest particle size combination). The calculated porosities based on grain density from mercury porosimetry ranged from 11.62% (thickest particle size combination) to 18.35% (finest particle size combination). The experimental porosities measured by gas porosimetry ranged from 10.32% (thickest particle size combination) to 14.67% (finest particle size combination), and the experimental porosities measured by mercury porosimetry ranged from 11.39% (thickest particle size combination) to 15.36% (finest particle size combination). Like the plugs composed of a 50% w/w particle size weight fraction, the porosities tended to decrease as the particle size increased.

In contrast to the observed trend in porosity, the experimental results of absolute permeability showed an increasing tendency with the increase in particle size. For plugs composed of a particle size weight fraction of 50% w/w:50% w/w, the experimental permeability by gas porosimetry ranged from 0.073mD (finest particle size combination) to 0.723mD (thickest particle size combination), while the experimental permeability by mercury porosimetry went from 0.021mD (finest particle size combination) to 0.274mD (thickest particle size combination). Similarly, for plugs composed of a particle size weight fraction of 25% w/w:75% w/w, the experimental permeability by gas porosimetry ranged from 0.112mD (finest particle size combination) to 0.717mD (thickest particle size combination). The experimental permeability by mercury porosimetry went from 0.038mD (finest particle size combination) to 0.289mD (thickest particle size combination).

Equation 1 indicates that porosity is affected by volume, grain density, and mass. As the resultant synthetic plugs had similar grain density, mass, and diameter, the decrease in height due to increasing particle size impacted porosity. When the combined particle size increased, the difference in size between particles became greater, decreasing sphericity and increasing the surface irregularity. Consequently, smaller particles may fill the pores between larger particles, reducing the overall volume occupied by particles and leading to decreased porosity and increased permeability.

As per the results discussed earlier, the porosities and permeabilities of the synthetic carbonate plugs are within the desired petrophysical range for porosity and permeability, similar to that of some of the pre-salt oil fields in Brazil. These fields exhibit 6%–28%

**Table 6**
Petrophysical analyses concerning calculated porosity, experimental grain density, porosity, and absolute permeability by gas and mercury porosimetry.

| | | Gas porosimetry | | | | | | Mercury porosimetry | | | |
|---|---|---|---|---|---|---|---|---|---|---|---|
| | Sample | Grain density (g/cm³) | Calculated porosity (%) based on gas porosimetry density | Experimental porosity (%) | Average experimental porosity used to plot Error! Reference source not found. | Experimental absolute permeability (mD) | Average experimental permeability used to plot Error! Reference source not found. | Grain density (g/cm³) | Calculated porosity (%) based on mercury | Experimental porosity (%) | Experimental absolute Permeability (mD) |
| | **100 g of base material mixed in weight fractions of 50% w/w: 50% w/w and 5% w/w of bonding material, 6% w/w hydrogen chloride solution of pH 3** | | | | | | | | | | |
| Finest particle size combination | 1 | 2.63 | 19.24 | 17.07 | 17.15 | 0.073 | 0.083 | 2.6019 | 18.37 | 19.96 | 0.021 |
| | 2 | 2.63 | 19.88 | 17.23 | | 0.093 | | - | | - | - |
| | 3 | 2.64 | 15.77 | 13.18 | 13.48 | 0.461 | 0.455 | 2.5915 | 14.19 | 13.77 | 0.077 |
| | 4 | 2.61 | 15.27 | 13.77 | | 0.450 | | - | | - | - |
| | 5 | 2.65 | 14.27 | 11.72 | 11.91 | 0.600 | 0.589 | 2.6044 | 13.54 | 12.77 | 0.140 |
| | 6 | 2.61 | 13.33 | 12.11 | | 0.578 | | - | | - | - |
| Thickest particle size combination | 7 | 2.63 | 13.00 | 10.66 | 10.54 | 0.671 | 0.697 | 2.6466 | 12.77 | 11.27 | 0.274 |
| | 8 | 2.64 | 13.32 | 10.43 | | 0.723 | | - | | - | - |
| | **100 g of base material mixed in weight fractions of 25% w/w: 75% w/w and 5% w/w of bonding material, 6% w/w hydrogen chloride solution of pH 3** | | | | | | | | | | |
| Finest particle size combination | 9 | 2.64 | 18.49 | 14.67 | 14.55 | 0.131 | 0.121 | 2.6354 | 18.35 | 15.36 | 0.038 |
| | 10 | 2.64 | 18.62 | 14.43 | | 0.112 | | - | | - | - |
| | 11 | 2.65 | 14.97 | 12.04 | 12.65 | 0.423 | 0.410 | 2.6317 | 14.38 | 14.21 | 0.099 |
| | 12 | 2.62 | 14.79 | 13.27 | | 0.397 | | - | | - | - |
| | 13 | 2.66 | 15.09 | 10.85 | 11.12 | 0.656 | 0.590 | 2.6781 | 15.61 | 14.78 | 0.353 |
| | 14 | 2.63 | 14.32 | 11.40 | | 0.524 | | - | | - | - |
| Thickest particle size combination | 15 | 2.64 | 12.74 | 10.47 | 10.39 | 0.717 | 0.700 | 2.6065 | 11.62 | 11.39 | 0.289 |
| | 16 | 2.64 | 12.94 | 10.32 | | 0.683 | | - | | - | - |

porosities and permeabilities ranging from 0.1 to 10,000 mD [14–22].

To better understand the pore network within the synthetic plugs, the pore size distribution was analyzed using mercury porosimetry [43]. This involved injecting mercury into the pores at increasing pressures and measuring the cumulative volume of mercury injected. Fig. 3 presents the pore size distribution of the synthetic plugs conformed by particle size weight fraction of 50% w/w:50% w/w (the part A) and 25% w/w:75% w/w (the part B). The results of this analysis revealed that the pore size distribution of the plugs fell within the mesoporosity range (0.5–5 μm) and microporosity range (<0.5 μm), which, although it does not cover all the range of typical carbonate rocks according to the classification presented by Schlumberger [11]. When porous reaches a micropore size, it promotes fluid trapping and irreducible fluid saturation [46]. Future analyses, such as mechanically forced fluid displacement, are recommended further to study this phenomenon in the resulting synthetic samples. In addition, peaks in the distribution indicated higher concentrations of pores of similar sizes at specific points. However, the absence of macroporosities suggested that the samples did not have vuggy-type and fracture-type porosities, common in carbonate rocks [47].

To obtain a more comprehensive understanding of the distribution of pores and bonding material within the synthetic plugs, two samples were chosen for analysis by SEM and micro-CT. Sample 1 with the finest particle size (composed of 50% w/w of particles smaller than 0.02 mm and 50% w/w of particles between 0.02 and 0.074 mm), while the other sample, the 7, composed of the coarser particle size (composed of 50% w/w of particles between 0.15 and 0.3 mm and 50% w/w of particles between 0.3 and 0.6 mm). Sample 1 was examined using micro-CT, while sample 7 was examined using SEM and micro-CT. Fig. 4 presents the SEM results of semi-qualitative microchemical analyses using backscattered electron and secondary electron imaging.

In Fig. 4A, four distinct points are visible, each displaying different levels of density and atomic number. The color of each point is

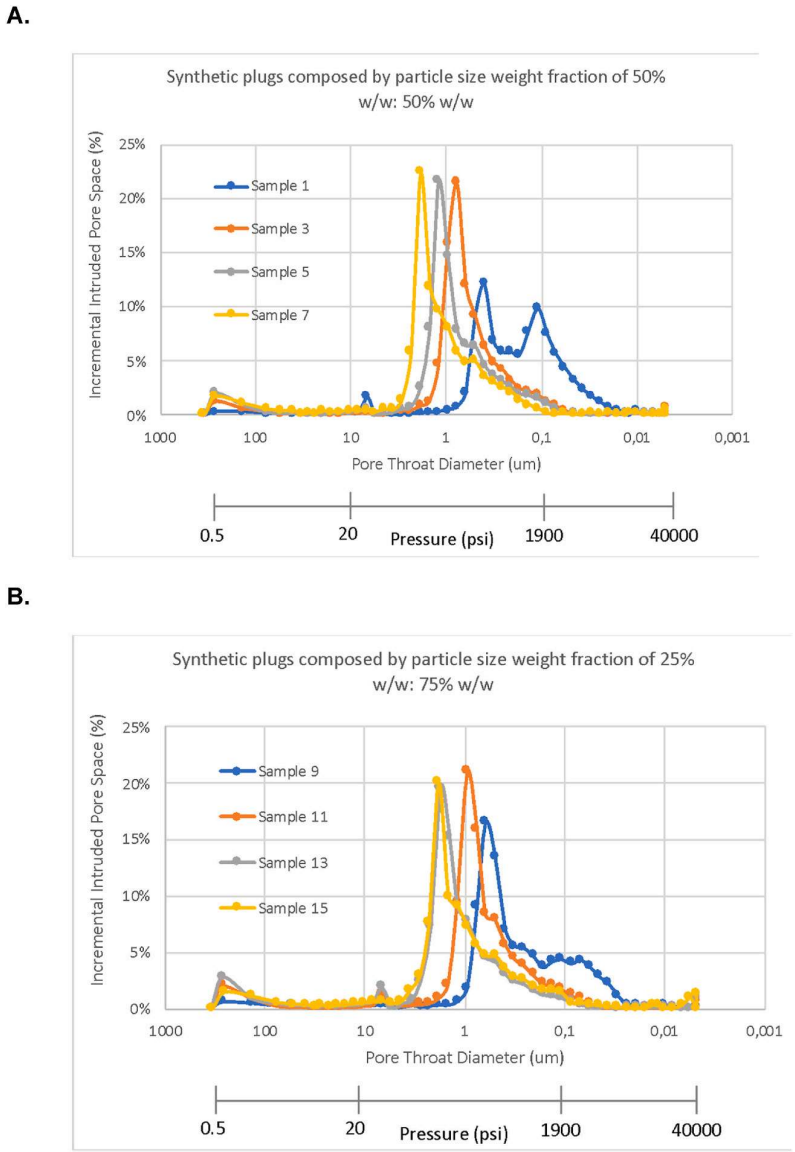


**Fig. 3.** Pore size distribution of the synthetic plugs conformed by particle size weight fraction of 50% w/w:50% w/w (A) and 25% w/w:75% w/w (B).

darker when its density and atomic number are lower. The images acquired at points 1, 2, and 4 revealed a higher concentration of calcium, magnesium, and oxygen, indicating the presence of the base material (dolomite rock) used to create the synthetic plug. However, point 3 showed a lower atomic number and a higher concentration of carbon, suggesting the presence of the bonding material used to create the plug. The increased concentration of carbon at point 3 could be attributed to the carbon compound used in the bonding material.

Fig. 4B depicts a magnified view of point 3 in Fig. 4A, highlighting bonding material within the synthetic plug. Similar to the previous analysis, a higher concentration of carbon was detected in the bonding material, indicating the presence of carbon-based compounds. Additionally, the SEM-EDS analysis revealed the presence of chlorine, which may have originated from the cold-mounted (embedded in epoxy resin) used during sample preparation for SEM-EDS analysis. Interestingly, the acquired image suggests the possible existence of voids within the bonding material region, which could potentially affect the porous network of the synthetic plug.

Two microtomography analyses were employed in this work: macro (pixel size of 20.5 μm) and micro (pixel size of 2 μm). From a macro scale point of view, microtomography analysis was employed to visualize the internal distribution of bonding material. Based on

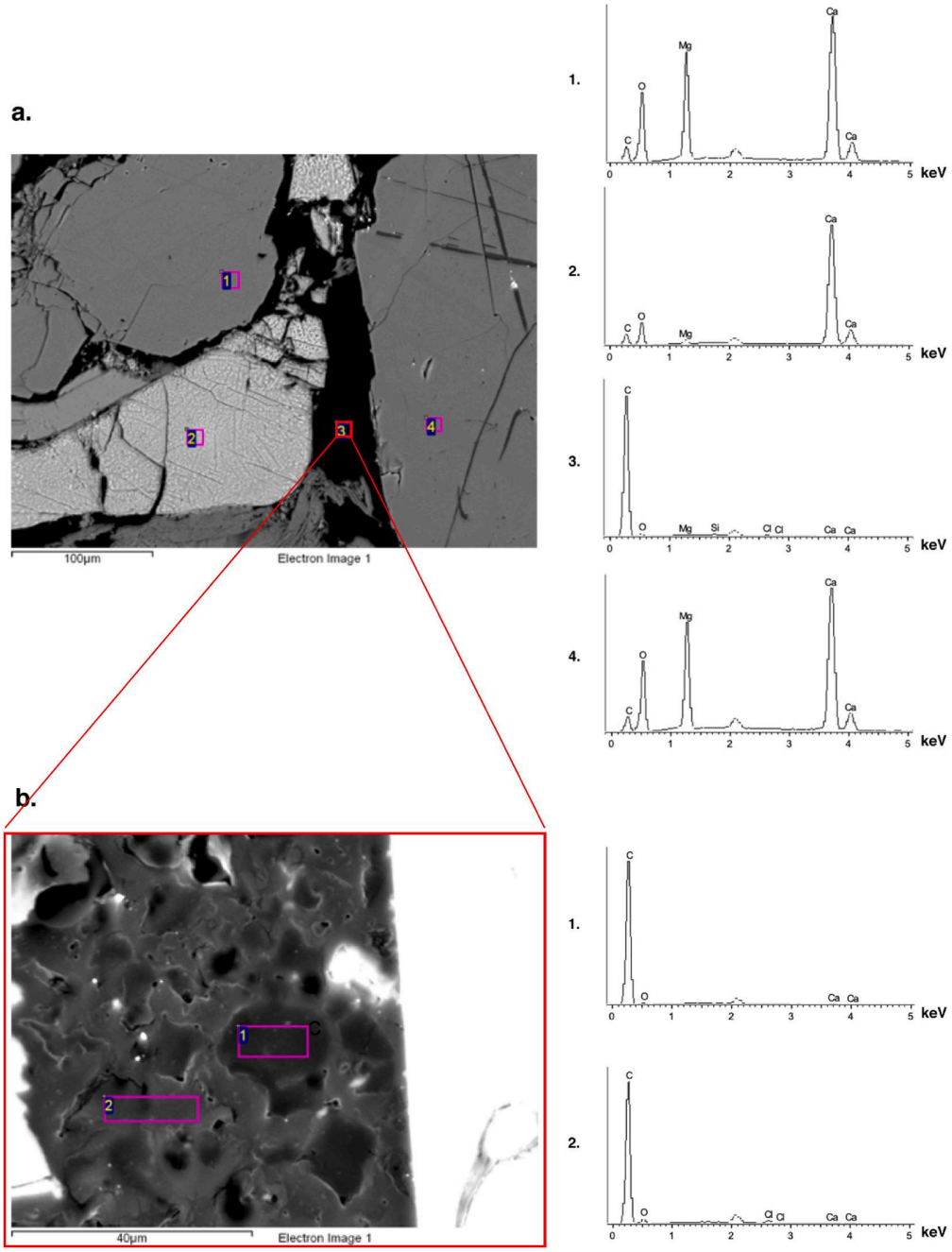


**Fig. 4.** Microchemical analysis of the acquired image by the SEM analysis using backscattered electron (part A) and secondary electron (part B) of sample 7 composed by 50% w/w of 0.15–0.3 mm, 50% w/w of 0.3–0.6 mm and, 5% w/w of bonding material, 6% w/w hydrogen chloride solution of pH 3.

the previous results of SEM, where it was corroborated the presence of bonding material between the particles of the base material, the acquired images were processed and separated into two phases: phase 1, which depicts the rock particles in grayscale, and phase 2, which shows the bonding material in blue for the sample composed by the finest combination of particle size (see Fig. 5, the part A) and the sample composed by the thickest combination of particle size (see Fig. 5 the, part B).

From phase 1, visual differences in the rock particles were observed from the two samples, which are expected to correspond to the

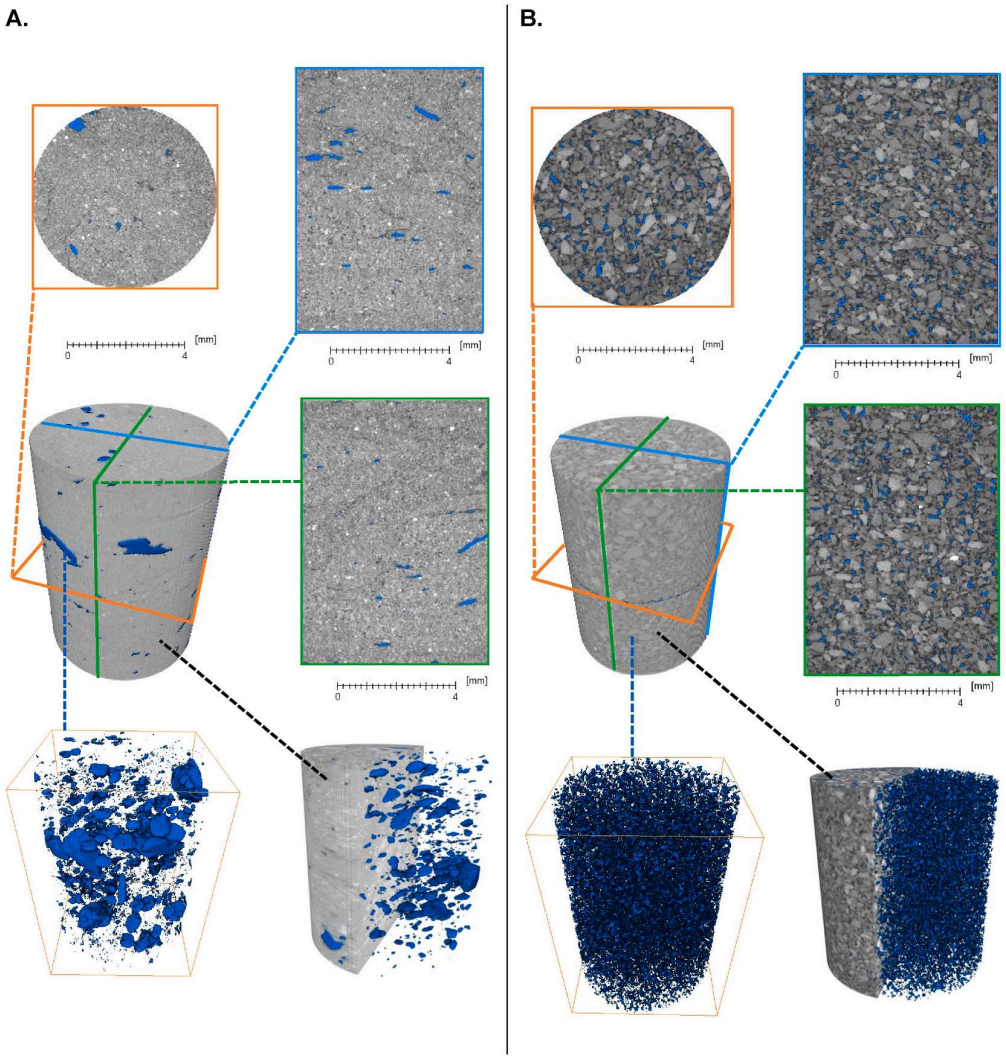


**Fig. 5.** Acquired micro-CT images from a macro scale point of view. Sample 1 (A) is composed of the finest combination of particle size 50% w/w of <0.02 mm, 50% w/w of 0.02–0.074, 5% w/w of bonding material, 6% w/w hydrogen chloride solution of pH 3, and; sample 7 (B) is composed of the thickest particle size 50% w/w of 0.15–0.3 mm, 50% w/w of 0.3–0.6 mm, 5% w/w of bonding material, 6% w/w hydrogen chloride solution of pH 3, separated into two phases: phase 1 rock particle in grayscale and phase 2 bonding material in color blue. (For interpretation of the references to color in this figure legend, the reader is referred to the Web version of this article.)

finest and coarse particle sizes used in samples 1 and 7, respectively. Furthermore, phase 2 in sample 1 (composed of the finest combination of particle size) exhibited larger conglomerates than phase 2 in sample 7 (composed of the thickest particle size), displaying a uniform visual distribution. These results may be corroborated by the comparative distribution analysis of the bonding material in the two samples, based on the macro analysis from microtomography shown in Fig. 6, where it is possible to observe a more homogeneous distribution localized around the finest equivalent diameters for sample 7 than sample 1. This behavior may probably be due to the particle accommodation filling empty spaces, thus reducing the bulk volume occupied and a better distribution of the bonding material.

From a micro-scale point of view, microtomography analysis was employed to visualize the internal distribution of the porous network. Based on the pore size distribution obtained by mercury porosimetry analyses, pores fell within the mesoporosity range (0.5–5 μm) and microporosity range (<0.5 μm) [11]. In this way, it was necessary to enhance the acquisition conditions of the analysis to improve the pixel size. Given the limitations imposed by the sample volume and the technique, increasing the pixel size from 20.5 μm to a maximum of 2 μm became feasible. Considering the concept of voxel size, which defines the size within a three-dimensional space region, it became possible to discern image details larger than 6 μm [48]. However, it is important to note that this acquisition condition is constrained and does not allow for the analysis of the sample's pores, as it falls outside the range the mercury porosimetry

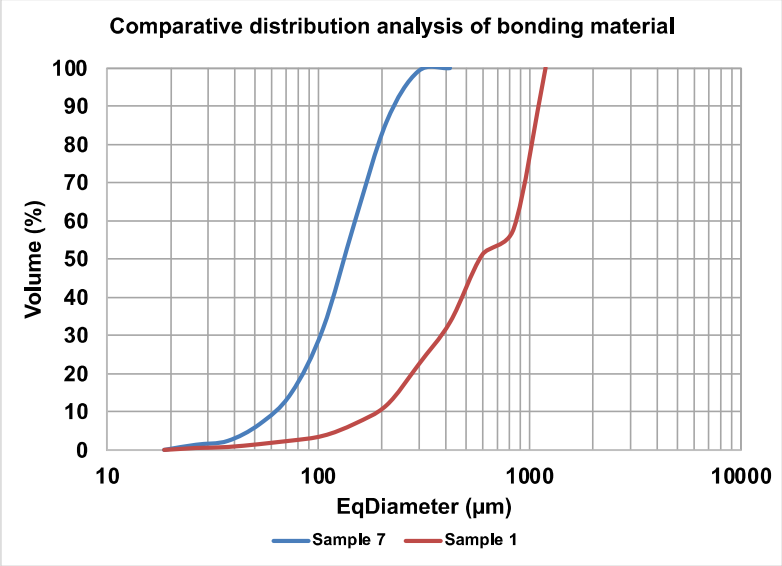


**Fig. 6.** Comparative distribution analysis of the bonding material in samples 1 and 7, based on the macro analysis from microtomography.

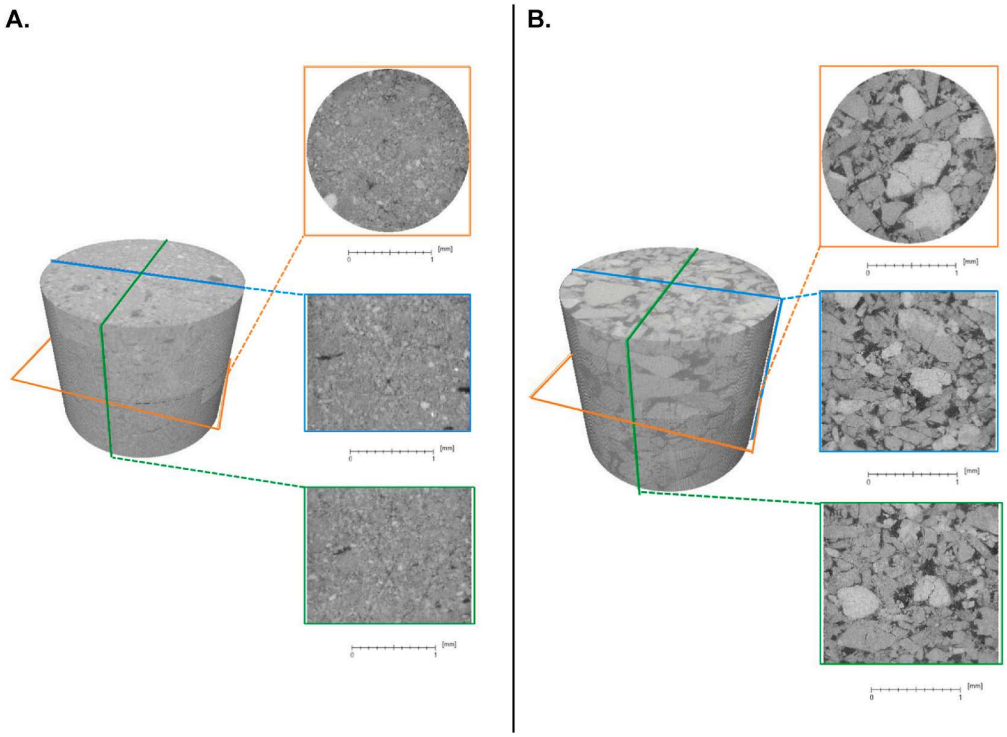


**Fig. 7.** Acquired micro-CT images from a micro-scale point of view.
Sample 1 (A) is composed of the finest combination of particle size 50% w/w of <0.02 mm, 50% w/w of 0.02–0.074, 5% w/w of bonding material, 6% w/w hydrogen chloride solution of pH 3, and; sample 7 (B) is composed of the thickest particle size 50% w/w of 0.15–0.3 mm, 50% w/w of 0.3–0.6 mm, 5% w/w of bonding material, 6% w/w hydrogen chloride solution of pH 3.

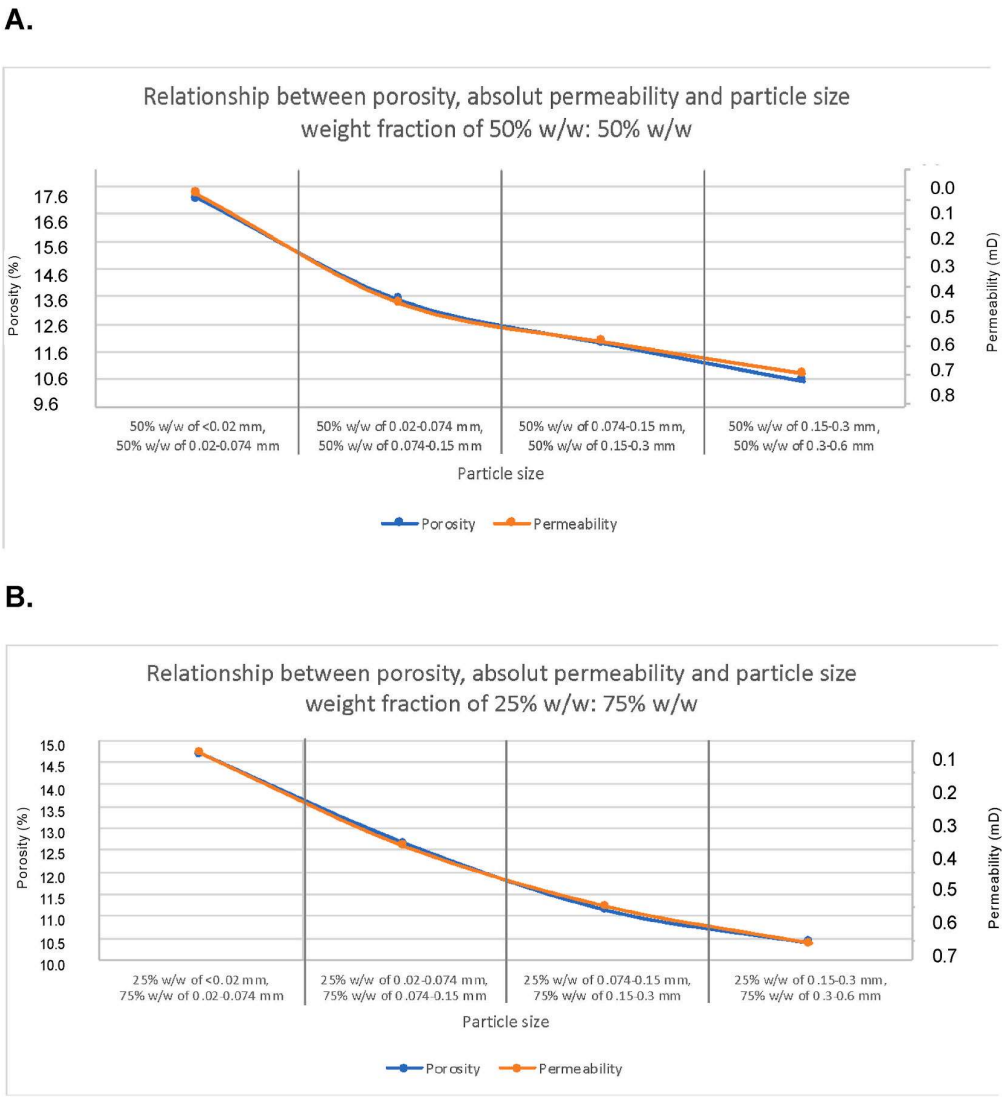


**Fig. 8.** Correlation between porosity, absolute permeability, and particle size weight fraction of 50% w/w:50% w/w (A) and 25% w/w:75% w/w (B).

technique detected. To address this limitation, an alternative approach could involve examining the resultant samples using nuclear magnetic resonance (NMR), as demonstrated by Morais [39]. In their study, NMR was able to visualize small pores (with an estimated size of 1.5 μm) in synthetic rocks, as opposed to X-ray micro-computed tomography. This complementary analysis, utilizing diffusion coefficients and relaxation times, can be correlated with the geometry and size of rock pores, facilitating the determination of porosity, predicting permeability, and enabling in-depth investigations into irreducible water saturations [39,49,50]. Fig. 7 presents the resulting image acquired by this condition, evidencing a limitation of the technique to identify the pore network in both samples composed by the finest combination particle size (Fig. 7, the part A) and the thickest particle size (Fig. 7, the part B).

As mentioned previously, the properties of the particles impacted their arrangement within the bulk volume, which, in turn, altered the synthetic plug's porosity and permeability. This suggests that the physical characteristics of the particles, such as their shape and size, play a crucial role in controlling the petrophysical properties of rocks. Therefore, understanding the relationship between particle and petrophysical properties is essential for predicting fluid flow through rocks and evaluating their suitability for various applications. To facilitate the controlled formation of synthetic carbonate plugs with a desired pore structure, the average porosity and absolute permeability results obtained from gas porosimetry were plotted against particle size and particle size weight fraction of 50% w/w:50% w/w (Fig. 8, the part A) and 25% w/w:75% w/w (Fig. 8, the part B). This allows observing a clear relationship between increased particle size, decreased porosity, and increased permeability.

## 4. Conclusion

From a mineralogical point of view, the reproduction of synthetic plugs similar to the rocks from oilfields may be achieved by using disintegrated dolomite rock as a base material, lower content of bonding material, and solubilization/precipitation methodology based on acid solution and temperature.

The relationship between particle size (0.3–0.6 mm, 0.15–0.3 mm, 0.074–0.15 mm, 0.02–0.074 mm and <0.02 mm), particle size weight fraction (50% w/w:50% w/w or 25% w/w:75% w/w), 5% w/w of bonding material, 6% w/w hydrogen chloride solution of pH 3 and drying temperature at 100 °C was evaluated, and the resulting synthetic plugs showed controlled petrophysical properties. The increasing particle size decreases porosity and increases permeability. These results highlight the influence of the particle shape (sphericity and surface irregularity) in the accommodation of particles in porous spaces.

Synthetic plugs evidenced heterogeneity (mesoporosities and microporosities) and variable petrophysical properties (porosities from 10% to 17% and 11%–19% from gas and mercury porosimetry, respectively, and permeabilities from 0.07 mD to 0.70 mD and 0.02 mD to 0.35 mD from gas and mercury porosimetry respectively) within the range of carbonatic Brazilian oilfield (porosities between 6% and 28%, permeabilities between 0.1 and 10,000 mD).

The comprehensive examination of the petrophysical properties of synthetic carbonate plugs presented in this study, the methodology, and the novel correlations proposed can contribute to the controlled formation of synthetic plugs with desired petrophysical properties, including porosity and permeability.

## Data availability statement

Data will be made available on request.

## Credit author statement

Jhonatan Jair Arismendi Florez: conceived and designed the experiments; performed the experiments; analyzed and interpreted the data; wrote the paper. Mateus Michelon: performed the experiments; analyzed and interpreted the data; wrote the paper. Carina Ulsen: conceived and designed the experiments; contributed reagents, materials, analysis tools or data; wrote the paper. Jean Vicente Ferrari: conceived and designed the experiments; performed the experiments; analyzed and interpreted the data; contributed reagents, materials, analysis tools or data; wrote the paper.

## Declaration of competing interest

The authors declare that they have no known competing financial interests or personal relationships that could have appeared to influence the work reported in this paper.

## Acknowledgements

Authors would like to thanks to LCT-Laboratorio de Caracterização Tecnologica, InTRA-Integrated Technology for Rock and Fluid Analysis, Fundo Patrimonial Amigos da Poli from the Universidade de São Paulo, Petrobras S.A and Poliplugs for the laboratory facilities, funding support, knowledge and materials used to develop this work.

## References

[1] J. Schon, Physical Properties of Rocks: A Workbook, vol. 8, [s.l.] Elsevier, 2011.
[2] R.A. Silva, M. Ceia, R. Missagia, I.A.L. Neto, Analysis of elastic velocities behavior and porosity in carbonates submitted to external pressure variation, J. Appl. Geophys. 166 (jul. 2019) 10–21.
[3] N. Watanabe, H. Kusanagi, T. Shimazu, M. Yagi, Local non-vuggy modeling and relations among porosity, permeability and preferential flow for vuggy carbonates, Eng. Geol. 248 (jan. 2019) 197–206.
[4] Z. Tariq, M. Mahmoud, H. Al-Youssef, M.R. Khan, Carbonate rocks resistivity determination using dual and triple porosity conductivity models, Petroleum 6 (1) (mar. 2020) 35–42.
[5] V.K. Bust, J.U. Oletu, P.F. Worthington, The challenges for carbonate petrophysics in Petroleum resource estimation, SPE Reservoir Eval. Eng. 14 (1) (21 fev. 2011) 25–34.
[6] G. Wang, P. Li, F. Hao, H. Zou, L. Zhang, X. Yu, Impact of sedimentology, diagenesis, and solid bitumen on the development of a tight gas grainstone reservoir in the Feixianguan Formation, Jiannan area, China: implications for gas exploration in tight carbonate reservoirs, Mar. Petrol. Geol. 64 (jun. 2015) 250–265.
[7] J. Lai, X. Pang, Q. Xiao, Y. Shi, H. Zhang, T. Zhao, Z. Qin, Prediction of reservoir quality in carbonates via porosity spectrum from image logs, J. Petrol. Sci. Eng. 173 (fev. 2019) 197–208.
[8] V.K. Bust, J.U. Oletu, P.F. Worthington, The challenges for carbonate petrophysics in Petroleum resource estimation, SPE Reservoir Eval. Eng. 14 (1) (21 fev. 2011) 25–34.
[9] K.S. Sing, et al., Pure Appl. Chem. 603 (1985).
[10] S. Lowell, J.E. Shields, M.A. Thomas, M. Thommes, Characterization of Porous Solids and Powders: Surface Area, Pore Size and Density, [s.l.] Springer, 2004.
[11] SCHLUMBERGER, Quantitative producibility and textural analysis for carbonate reservoirs, in: Carbonate Advisor, 2008. Available: https://www.slb.com/-/media/files/fe/brochure/carbonate-advisor-br. Accessed January 2023.
[12] S. Mineo, G. Pappalardo, InfraRed Thermography presented as an innovative and non-destructive solution to quantify rock porosity in laboratory, Int. J. Rock Mech. Min. Sci. 115 (mar. 2019) 99–110.
[13] Peter C. Hewlett, L.E.A. Frederick Measham, Lea's Chemistry of Cement and Concrete, fourth ed., 1998. Microsilica as an addition. 12.6.4 Permeability.

[14] ANP (2018) Badejo reservoir. Available: <http://www.anp.gov.br/images/EXPLORACAO_E_PRODUCAO_DE_OLEO_E_GAS/Gestao_Contratos/Fase_Producao/Planos_Desenvolvimento/Sumario_Executivo_Externo_Badejo.pdf>. Accessed December 2022.
[15] ANP (2018) Bicudo reservoir. Available: http://www.anp.gov.br/images/planos_desenvolvimento/Bicudo.pdf. Accessed December 2022.
[16] ANP (2018) Bonito reservoir. Available: <http://www.anp.gov.br/images/planos_desenvolvimento/Bonito.pdf>. Accessed December 2022.
[17] ANP (2018) Garoupa reservoir. Available: <http://www.anp.gov.br/images/planos_desenvolvimento/Garoupa.pdf>. Accessed December 2022.
[18] ANP (2018) Linguado reservoir. Available: <http://www.anp.gov.br/images/planos_desenvolvimento/Linguado.pdf>. Accessed December 2022.
[19] ANP (2018) Pampo reservoir. Available: <http://www.anp.gov.br/images/planos_desenvolvimento/Pampo.pdf>. Accessed December 2022.
[20] ANP (2018) Piranema reservoir, Available: <http://www.anp.gov.br/images/planos_desenvolvimento/Piranema.pdf>. Accessed December 2022.
[21] ANP (2018) Siri reservoir. Available: <http://www.anp.gov.br/images/planos_desenvolvimento/Siri.pdf>. Accessed December 2022.
[22] ANP (2018) Trilha reservoir. Available: <http://www.anp.gov.br/images/planos_desenvolvimento/Trilha.pdf>. Accessed on December 2022.
[23] Patrick Murphy, D. V.;Chilingarian, G.; Jalal Torabzadeh, S. Chapter 3 Core Analysis and its Application in Reservoir Characterization. In: [s.l: s.n.]. p. 105–153.
[24] I.A.M. Salifou, H. Zhang, I.O. Boukari, M. Harouna, Z. Cai, New vuggy porosity models-based interpretation methodology for reliable pore system characterization, Ordovician carbonate reservoirs in Tahe Oilfield, North Tarim Basin, J. Petrol. Sci. Eng. 196 (2021), 107700.
[25] J. Hook, An Introduction to Porosity. Petrophysics. Society of Petrophysicists and Well-Log Analysis, V. 44, N. 3, Paper Number: SPWLA-2003-V44n3a4, 2003.
[26] M.J. Church, Grain size and shape, in: Sedimentology, Springer Netherlands, Dordrecht, 2013, pp. 544–554.
[27] Horiba. A Guidebook to Particle Size Analysis. Available: < https://static.horiba.com/fileadmin/Horiba/Products/Scientific/Particle_Characterization/Particle_Guidebook_2022.pdf>. Accessed January 2023.
[28] F. Massad, Mecânica Dos Solos Experimental, [s.l.] Oficina de textos, 2016.
[29] J.L. Laxton, A particle-size classification of sand and gravel deposits as a basis for end-use assessment, Eng. Geol. 32 (1–2) (fev. 1992) 29–37.
[30] M.J. Church, Grain size and shape, in: Sedimentology, Springer Netherlands, Dordrecht, 2013, pp. 544–554.
[31] J.J. Arismendi Florez, J.V. Ferrari, M. Michelon, C. Ulsen, Construction of synthetic carbonate plugs: a review and some recent developments, Oil & Gas Science and Technology – Revue d'IFP Energies Nouvelles 74 (29) (mar. 2019), 20.
[32] K. Bjorlykke, J. Jahren, N.H. Mondol, O. Marcussen, D. Croize, C. Peltonen, B. Thyberg, Sediment Compaction and Rock Properties. AAPG International Conference and Exhibition, 2009. Available: https://www.researchgate.net/profile/Nazmul-Mondol/publication/228823690_PS_Sediment_Compaction_and_Rock_Properties/links/0fcfd5110dcbf5ff9d000000/PS-Sediment-Compaction-and-Rock-Properties.pdf. Accessed February 2023.
[33] H. Wang, W. Xu, J. Zuo, Compact rock material gas permeability properties, Phys. B 449 (2014) 10–18.
[34] Q. Ran, Y. Wang, Y. Sun, L. Yan, M. Tong, Volcanic reservoir mode, in: Development of Volcanic Gas Reservoirs, [s.l.] Elsevier, 2019, pp. 115–265.
[35] J.B. Regnet, C. David, P. Robion, B. Menendez, Microstructures and physical properties in carbonate rocks: a comprehensive review, Mar. Petrol. Geol. 103 (2019) 366–376.
[36] D.R. Montgomery, D. Zabowski, F.C. Ugolini, R.O. Hallberg, H. Spaltenstein, Soils, watershed processes, and marine sediments, 159–iv, in: Earth System Science: from Biogeochemical Cycles to Global Changes 72, 2000.
[37] J.J. Arismendi Florez, J.V. Ferrari, Preliminary analyses of synthetic carbonate plugs: consolidation, petrophysical and wettability properties, Oil & Gas Science and Technology – Revue d'IFP Energies Nouvelles 76 (9 fev. 2021) 12.
[38] M.M. Morais, R.D. Salomao, C.A. Fortulan, Successful and failed attempts to obtain bulk calcium carbonate parts through sintering and carbonation, in: Proceedings. 65-66 Congresso Brasileiro de Cerâmica, Associação Brasileira de Cerâmica, 2022.
[39] M.M. Morais, E. Lucas-Oliveira, T.J. Bonagamba, P.T.P. Aum, C.R.D.S. Lucas, D.N.D.N.D. Silva, C. Fortulan, Fabrication and petrophysical characterization of artificial carbonate rocks with multiscale porosity sintered in a Co2 atmosphere, Geoenergy Sci. Eng. 229 (2022). Preprint SSRN Electronic Journal.
[40] H. Azari, E. Garboczi, Optical Sizing and Roundness Determination of Glass Beads Used in Traffic Markings: A Summary, National Academies Press, Washington, D.C., 2010.
[41] K.L. Jones, G.P. Matthews, G.M. Laudone, The effect of irradiation and radiolytic oxidation on the porous space of Gilsocarbon nuclear graphite measured with mercury porosimetry and helium pycnometry, Carbon 158 (mar. 2020) 256–266.
[42] C. Voigt, J. Hubalkova, H. Giesche, C.G. Aneziris, Intrusion and extrusion mercury porosimetry measurements at Al2O3–C - influence of measuring parameter, Microporous Mesoporous Mater. 299 (2020), 110125.
[43] R. Qian, J. Shi, C. Liu, G. Liu, Z. Liu, W. She, Y. Liang, Investigations on pore-structure in cementitious materials using gas intrusion porosimetry, Meas. J. 171 (2021).
[44] WEBMINERAL. Dolomite mineral data. Available: < http://webmineral.com/data/Dolomite.shtml#.ZErGLC-B3RY>. Accessed March 2023.
[45] I. Krupa, Z. Nogellova, Z. Spitalsky, M. Malikova, P. Sobolciak, H.W. Abdelrazeq, M.A.S. Al-Maadeed, Positive influence of expanded graphite on the physical behavior of phase change materials based on linear low-density polyethylene and paraffin wax, Thermochim. Acta 614 (2015) 218–225.
[46] M.S. El Sharawy, G.R. Gaafar, Impacts of petrophysical properties of sandstone reservoirs on their irreducible water saturation: implication and prediction, J. Afr. Earth Sci. 156 (2019) 118–132.
[47] L. Liu, W. Fan, X. Sun, Z. Huang, J. Yao, Y. Liu, X. Wang, Gas condensate well productivity in fractured vuggy carbonate reservoirs: a numerical modeling study, Geoenergy Sci. Eng. 225 (2023), 211694.
[48] L. Dong, J. Wang, D. Wang, Modeling and design of three-dimensional voxel printed lattice metamaterials, Addit. Manuf. (2023), 103532.
[49] A.T. Krzyzak, W. Mazur, A. Fheed, W.P. Weglarz, Prospects and challenges for the spatial quantification of the diffusion of fluids containing 1H in the pore system of rock cores, J. Geophys. Res. Solid Earth 127 (3) (2022).
[50] Trevizan, W.A. Nuclear magnetic resonance and digital rock in oil industry: well logging applications. Thesis presented to obtain the degree of Doctor of Science. Advisor: Prof. Dr. Tito José Bonagamba. Universidade de São Paulo. 2017. Available <https://teses.usp.br/teses/disponiveis/76/76131/tde-10080217-113902/en.php> Accessed June 2023.